Interaction between Lipid Monolayers and Poloxamer 188: An X-Ray Reflectivity and Diffraction Study

Guohui Wu,* Jaroslaw Majewski,† Canay Ege,* Kristian Kjaer,‡ Markus Jan Weygand,‡ and Ka Yee C. Lee*
*Department of Chemistry, the Institute for Biophysical Dynamics and the James Franck Institute, the University of Chicago, Chicago, Illinois; †Manuel Lujan Jr. Neutron Scattering Center, Los Alamos National Laboratory, Los Alamos, New Mexico; and ‡Materials Research Department, Risø National Laboratory, Roskilde, Denmark

ABSTRACT The mechanism by which poloxamer 188 (P188) seals a damaged cell membrane is examined using the lipid monolayer as a model system. X-ray reflectivity and grazing-incidence x-ray diffraction results show that at low nominal lipid density, P188, by physically occupying the available area and phase separating from the lipids, forces the lipid molecules to pack tightly and restore the barrier function of the membrane. Upon compression to bilayer equivalent pressure, P188 is squeezed out from the lipid monolayer, allowing a graceful exit of P188 when the membrane integrity is restored.

INTRODUCTION

In victims of electrical shock or lightning injury, altered membrane properties in response to strong electric field exposure appear to be directly relevant to tissue injury mechanisms. Electrical injuries to cell membrane can result in the following events: thermal burns secondary to Joule heating (1–3), permeabilization of cell membranes (4), and/or denaturation of macromolecules such as proteins (5). Electroporation (suggesting actual pore formation) and electropermeabilization (likely due to the loss of the innate lipid packing density) are the two terms commonly used to describe the biophysical process of enhanced membrane permeability due to electric field-driven reorganization of lipids in the lipid bilayer by supraphysiologic electric fields (6–8). Contemporary electroporation theory indicates that polar water molecules are pulled by Kelvin polarization stress into transient defects in the lipid packing order within a bilayer, leading to quasistable or stable pore formation (9–12).

A break in the integrity of the plasma membrane immediately compromises its essential role as a barrier, thereby severely affecting its control over the exchange of materials between the cell and its surrounding environment, which eventually causes cell death. Sealing of permeabilized cell membranes is therefore of vital importance to medical treatment of electrical shock victims.

The successful restoration of membrane transport properties through surfactant poloxamer 188 was first demonstrated in 1992 (2). Poloxamer 188 (P188, mol wt = 8400 g/mol), a member of a triblock copolymer family called poloxamers, or pluronics, has the structure of poly(ethylene oxide)-poly (propylene oxide)-poly(ethylene oxide) (PEO-PPO-PEO, with 80 wt % PEO content), and has a firmly established medical safety record since 1957. As a result of its amphiphilic nature, P188 has the capability to interact with a cell membrane and is found to alleviate as well as reverse damages caused by electrical trauma. It was demonstrated that P188 can seal cells against loss of carboxyfluorescein dye after electroporation (2,13–18). In the intervening years, P188 has been determined as a successful sealing agent for various permeabilized cells, such as skeletal muscle tissue after heat shock and intense irradiation (19,20), red blood cell from sickle cell disease (21), etc. Although these results show that P188 is effective in restoring damaged cell membranes, the underlying mechanisms have barely been studied until recently (22).

Besides being used as a sealing agent, poloxamers have also received much attention during the past decade for their application in drug delivery. It is known that liposomes (used as drug carriers) can be modified with poloxamers to prolong their circulation time in the blood stream as well as to prevent their flocculation, fusion, or binding (13–18). Although the mode of interaction between poloxamer and liposome has been hypothesized, it remains poorly understood.

Recently there have been studies to measure the ability of poloxamers to interact with model membranes (22,23), however, no effort has yet been made to elucidate the lipid/poloxamer interaction at the molecular level, which is critical in improving the design of poloxamers for medical applications. To gain insight into the mechanisms of interaction between poloxamer and damaged membrane, we have used a Langmuir lipid monolayer at the air-water interface as a model system and have performed a series of x-ray reflection (XR) and grazing incidence x-ray diffraction (GIXD) experiments to gain information at the molecular level.

The Langmuir lipid monolayer serves as a good model for the outer leaflet of the cell membrane. By controlling the surface area available for the lipid monolayer, the intact membrane (with tightly packed lipid molecules at the bilayer

Submitted September 3, 2004, and accepted for publication June 27, 2005.

Address reprint requests to Ka Yee C. Lee, Dept. of Chemistry, the Institute for Biophysical Dynamics and the James Franck Institute, the University of Chicago, 5735 S. Ellis Ave., Chicago, IL 60637. E-mail: kayeelee@uchicago.edu.

0006-3495/05/11/3159/15 $2.00

doi: 10.1529/biophysj.104.052290

equivalent pressure of 30–35 mN/m (24,25), as well as the disrupted portion of the membrane post-trauma (with low lipid density) can be effectively mimicked. The low-density lipid film at the air-water interface represents the hydrophobic-aqueous environment that the poloxamer sees on a damaged membrane. Such a hydrophobic-aqueous environment can be found both at the highly curved lipid portion that constitutes the pore, and in the portion of the membrane that has enhanced permeability due to a reduction in lipid density. Both sites have enhanced exposure of the lipid hydrocarbon tail to the aqueous environment, into which the poloxamer, being amphiphilic in nature, can possibly insert.

X-ray beams from intense and well collimated synchrotron sources have been used as a molecular probe for direct structural information on the organization of amphiphilic molecules at the air-water interface (26–29). Our earlier work has demonstrated that XR and GIXD can help gain insight into the interaction between lipid and poloxamer (30). Here we report detailed structural parameters for pure lipid and lipid/P188 monolayers at different surface pressures. To the best of our knowledge, these studies are the first complete in situ investigations providing quantitative information on the insertion of P188 into lipid monolayers, as well as the effect of P188 on the packing of lipid molecules. Our data also help to pinpoint the location of P188 in the lipid matrix.

MATERIALS AND METHODS

Materials

1,2-Dipalmitoyl-*sn*-glycero-3-phosphocholine (DPPC) and 1,2-dipalmitoyl-*sn*-glycero-3-[phospho-rac-(1-glycerol)] (DPPG) were purchased in powdered form from Avanti Polar Lipids (Alabaster, AL) and used without further purification. Monolayer spreading solutions were prepared by dissolving the solid lipid in either pure chloroform (for DPPC) or 9:1 v/v chloroform-methanol (for DPPG) to obtain a concentration of 0.5 mg/ml. Throughout the experiments, ultrapure water (resistivity $\geq$18 MΩ cm) obtained from a Milli-Q UV Plus system (Millipore, Bedford, MA) was used as the subphase.

P188 solution of 200 mg/ml was prepared by adding poloxamer (BASF, Parisippany, NJ) and ultrapure water to a vial containing a magnetic stir bar, and then left to mix on a stirplate for 0.5 h to ensure complete dissolution. The poloxamer solution was kept at 4°C before use, and made fresh every 2 weeks.

Experimental configuration

Surface-pressure area (Langmuir) isotherms were obtained with a home-built Langmuir trough equipped with a Wilhelmy plate (31). In a typical isotherm experiment, the lipid molecules dissolved in chloroform were deposited at low surface density at the air-water interface, leaving an initial surface pressure of 0 mN/m. The solvent was allowed to evaporate for 5–15 min. P188 was then injected into the subphase by inserting a syringe through the air-water interface, and the final P188 concentration was 50 μM in the subphase. All experiments were performed at 30°C. For isotherm measurements the compression was achieved with two barriers moving at a rate of 6.3 mm^2/s. Depending on the initial amount of material deposited at the interface, this translates to a lipid molecular area reduction rate between 0.04 and 0.06 Å$^2\cdot$s^{-1}.

Experiments were also performed at a synchrotron source. All x-ray scattering experiments were carried out at the BW1 (undulator) beam line at HASYLAB (Hamburg, Germany) using a dedicated liquid surface diffractometer (29,32–34) with an incident x-ray wavelength of $\lambda \sim 1.3$ Å. A thermostated trough equipped with a Wilhelmy balance for measuring the surface pressure (π) and a barrier for changing the surface area was mounted on the diffractometer.

Two types of x-ray scattering experiments were performed. The first set of experiments, referred to as pretreatment experiments in our previous work (22), was designed to study the pure lipid monolayer, as well as the interaction between P188 and lipid in a mixed film. The second set of experiments, aimed at studying the structure of P188 at the air-water interface, was performed in a manner similar to the first but with no lipid present. For both sets of experiments, after the sample was prepared but before x-ray data were collected at least 40 min were allowed for the trough enclosure to be flushed with helium to reduce the scattering background and to minimize beam damage during x-ray scans; x-ray data were collected afterward.

Both XR and GIXD were carried out to obtain out-of-plane as well as in-plane electron density distribution information on these samples. X-ray scattering theory and the liquid diffractometer used here have been described previously (26–29). The reflectivity data were analyzed using a kinematical approach (26,35). The electron density $\rho(z)$, which is laterally averaged over both the ordered and disordered parts in the footprint of the beam, can be modeled by a stack of homogeneous slabs (''boxes'') with each having a constant electron density and thickness. The interfaces between boxes are smoothed with a Gaussian function of standard deviation σ to account for roughness at the boundary due to thermally excited capillary waves and atomic roughness of the interface (36,37).

The GIXD intensity resulting from a powder of 2-D crystallites may be represented by its projection onto the q_{xy} axis to yield Bragg peaks or onto the q_z axis to yield Bragg rods, where q_{xy} and q_z are the horizontal and vertical components of the scattering vector q, respectively (26,35,38). The intensity distribution along a Bragg rod can be analyzed to infer the direction and magnitude of the molecular tilt in the crystalline part of the monolayer. In this work we model the lipid tail by a cylinder of constant electron distribution with adjustable parameters being the tilt angle of the cylinder from the vertical, the lateral tilt direction, the length of the cylinder, L_c (i.e., the length of the part of the molecule that scatters coherently), and the vertical root mean-square displacement, σ_z (Debye-Waller factor), in the crystallites. The horizontal positions of the Bragg peaks (q_{xy}) allow for the determination of the spacings $d = 2\pi/q_{xy}$ for the 2-D lattice of the alkyl chains. The width of Bragg peaks, corrected for the instrumental resolution, gives the finite size of the crystalline domains in the direction of the reciprocal scattering vector q_{xy} (the 2-D crystalline coherence length L_{xy}) (39).

The dimensions of the footprint of the incoming x-ray beam on the liquid surface were $\sim 2 \times 50$ mm^2. As a precaution against beam damage, in GIXD the trough was translated by 0.025 mm horizontally across the x-ray beam, in the direction along the barrier compression at every step of the q_{xy} scan; in XR, the sample was completely renewed by occasional translation of the full 2-mm width of the beam. Remeasuring part of the reflectivity curve before and after translation afforded a check of the reproducibility.

RESULTS

Isotherm

The effect of P188 on the phase behaviors of pure DPPC and DPPG monolayers was studied via isotherm measurements, and results are shown in Fig. 1, *A* and *B*, respectively. In the pretreatment experiments (22), the lipid was spread at a high area/lipid molecule ($\pi = 0$ mN/m), and P188 was added to the water subphase. For both lipid monolayers, the addition of P188 to the subphase resulted in the partitioning of P188 to the air-water interface, causing an instantaneous increase in surface pressures from 0 to ~22 mN/m; after waiting for

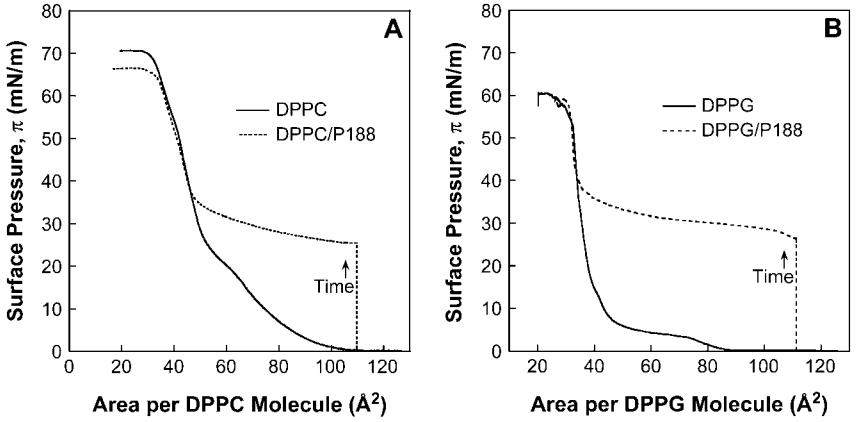

FIGURE 1 Lateral compression isotherms of (*A*) DPPC (*solid line*) and DPPC/P188 (*dashed line*) on a pure water subphase at 30°C. (*B*) DPPG (*solid line*) and DPPG/P188 (*dashed line*) on water subphase. For both the lipid/P188 systems, compression commenced 40 min after P188 injection. At surface pressures ≥36 mN/m for DPPC film, or ≥38 mN/m for DPPG film, the isotherms of the P188-treated systems overlap those of the pure lipids, indicating that P188 is ''squeezed out'' of the film at such surface pressures.

40 min to simulate conditions at the synchrotron source, the surface pressure further rose to 26 mN/m. Under this condition, fluorescence microscopy revealed surface heterogeneities at the length scale as large as ~15 mm as discussed in Appendix A. The lipid/poloxamer system was then compressed until collapse. Fig. 1, *A* and *B*, shows that as the DPPC monolayer was compressed to 36 mN/m and beyond, or DPPG to 38 mN/m and beyond, the isotherms of the poloxamer-pretreated monolayers reverted to those of the pure lipids and the surface heterogeneities were eliminated, suggesting that P188 is eliminated from the system. Although the isotherms provide macroscopic information on the lipid-poloxamer interaction as a function of surface pressure, XR and GIXD experiments are needed to provide details at the molecular level regarding the fate of the poloxamer at high surface pressures, and to pinpoint the location of the poloxamer in the lipid matrix as well as the subsequent effect on lipid ordering upon P188 insertion.

It should be noted that the adsorption of the injected poloxamer to the air-water interface is a time-dependent process. Fig. 2 shows the change with time in surface pressure of a DPPC/P188 film. The lipid was spread at a high area/DPPC molecule (A_{DPPC}) at 109.6 Å^2, resulting in a zero surface pressure. Upon the injection of P188 into the subphase, the surface pressure rose almost instantaneously from 0 to ~22 mN/m. After that, the surface pressure increased slowly to 26 mN/m in 40 min (see Appendix C).

As a control, the isotherm of pure P188 at the air-water interface was measured. P188 was injected into the subphase directly without any phospholipid monolayer spread at the air-water interface. After 40 min ($\pi = 26$ mN/m), the barrier compression was started and isotherm data were recorded. A weak dependence of surface pressure on area is observed: π increases from 26 to 29 mN/m with barriers compressed from a maximum trough area of 438 cm^2 to the minimum of 109 cm^2.

GIXD and XR of poloxamer 188

X-ray scattering experiments were performed on pure P188 films with the same experimental condition as that for isotherm measurements except that x-ray measurements were carried out during the compression of P188 film. XR and GIXD were measured at $\pi = 26$, 27, and 29 mN/m, corresponding to the maximum, intermediate, and minimum trough area, respectively. Bragg peaks were absent for all the investigated conditions when only polymer was present in the water subphase.

The x-ray reflectivity data for pure P188 in a water subphase at 30°C are shown in Fig. 3. The reflectivity profile of P188 is very similar to that of the bulk water subphase, and can be fitted by a one-box model, with a thickness of 21.6 ± 1.0 Å and normalized electron density of 1.04 ± 0.01. (All electron densities ρ reported are normalized to that of the water subphase, $\rho_{water} = 0.334e^-/Å^3$.) Although the increase of surface pressure upon the addition of P188 clearly shows the presence of the polymer at the air-water interface, the low electron density contrast between P188 and water causes a very small deviation in the reflectivity of P188 (R) from that of the free surface of water (the Fresnel curve augmented with interfacial roughness $\sigma \sim 3$ Å, giving

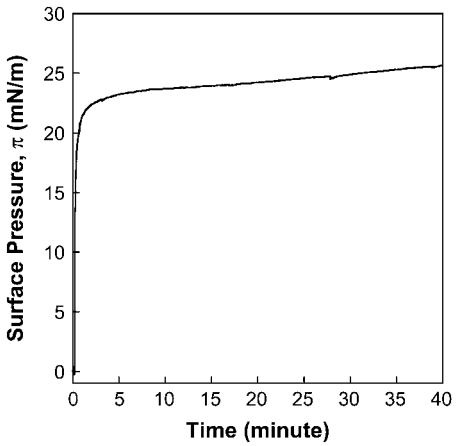

FIGURE 2 Change in surface pressure for a P188-treated DPPC monolayer on a water subphase at 30°C with time. P188 was introduced into water subphase at time = 0 when the pure lipid film gave a surface pressure of 0 mN/m.

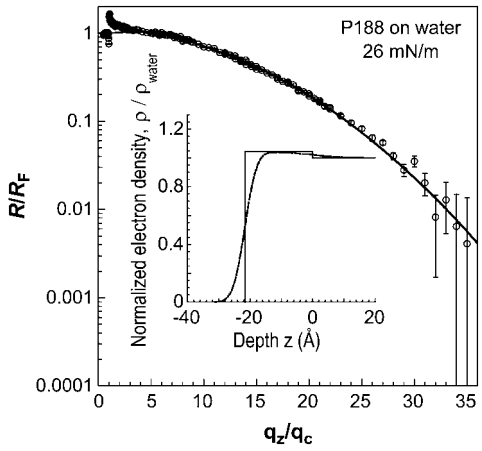

FIGURE 3 X-ray reflectivity data and fit for P188 at the air-water interface at 30°C. The double cusp of R/R_F near $q_z = q_c$ is an artifact. It comes from dividing the measured $R(q_z)$ (which is affected by finite resolution) by the ideally calculated Fresnel law $R_F(q_z)$. Therefore, only data for $q_z > 3q_c$ were included in the analysis. The inset is the corresponding normalized electron density profile $\rho(z)/\rho_{water}$ in smeared (by interfacial roughness) and unsmeared forms. $z = 0$ signifies the start of the water subphase.

a reflectivity $R_F\, e^{-q_z^2\sigma^2}$). The low contrast is seen in the fitted parameter $\rho_{P188}/\rho_{H2O} = 1.04 \pm 0.01$. The fitting results also show that the P188-water interface ($\sigma = 7.9 \pm 1.0$ Å) is much rougher than the air-P188 interface ($\sigma = 3.0 \pm 0.1$ Å). Such roughness precludes the observation of any fringe corresponding to ~22 Å thick P188 layer in the XR data.

Grazing-incidence x-ray diffraction

Pure DPPC

GIXD measurements provide in-plane structural information on the crystalline, diffracting portion of the monolayer. Fig. 4, *A* and *B*, shows Bragg peaks for a pure DPPC and P188-treated DPPC monolayer, respectively, at various areas/lipid molecule. The structural parameters are summarized in Table 1. In Fig. 4 *A*, a pure DPPC monolayer at $A_{DPPC} = 63$ Å^2 exhibits no Bragg peak, indicating the lack of any lipid ordering. Compression to $A_{DPPC} = 58$ Å^2 results in a similarly flat profile, though some features (still within the noise level) are becoming discernable.

At $A_{DPPC} = 48$ Å^2, two Bragg peaks are observed at $q_{xy} = 1.38$ Å^{-1} and 1.46 Å^{-1}. The pattern thus consists of two low-order reflections, indicating a distorted-hexagonal cell (see Appendix D). The integrated intensity of the Bragg peak at $q_{xy} = 1.38$ Å^{-1} is roughly twice that of the peak at $q_{xy} = 1.46$ Å^{-1}. This higher intensity results from coincident four reflections $\{(10), (\bar{1}0), (01), (0\bar{1})\}$ (simplified as $\{10,01\}$) versus two reflections $\{(1\bar{1}), (\bar{1}1)\}$(simplified as $\{1\bar{1}\}$) and leads to the assignment of the $\{10,01\}$ reflection to the $q_{xy} = 1.38$ Å^{-1} peak and the $\{1\bar{1}\}$ reflection to the $q_{xy} = 1.46$ Å^{-1} peak. The spacings ($d_{xy} = 2\pi/q_{xy}$) are $d_{10,01} = 4.55$ Å and $d_{1\bar{1}} = 4.30$ Å, giving rise to a distorted hexagonal unit cell with axes $|a| = |b| = (2d_{1\bar{1}}^2)/\left(\sqrt{(2d_{1\bar{1}})^2 - d_{10,01}^2}\right) = 5.07$ Å and $\gamma = 2\arctan\left(\sqrt{(2d_{1\bar{1}})^2 - d_{10,01}^2}/d_{10,01}\right) = 116°$, and a unit cell area (containing one chain), A_{30}, of 23.1 Å.

When resolved in both q_{xy} and q_z (cf. Figs. 5 *A* and 6 below), the peak at $q_{xy} = 1.38$ Å^{-1} can be seen to consist of two barely resolved peaks, indicating that the lattice is oblique (see Appendix E). However, in this report this splitting is ignored for simplicity, leading to a distorted-hexagonal lattice, as indicated above. This holds true for the rest of DPPC films investigated in our system.

The corresponding full widths at half-maximum height (FWHM) of the two peaks are $FWHM_{meas}(q_{10,01}) = 0.105$ Å^{-1} and $FWHM_{meas}(q_{1\bar{1}}) = 0.026$ Å^{-1}, both of which exceed the instrumental resolution of $FWHM_{resol}(q_{xy}) = 0.0084$ Å^{-1}. The intrinsic FWHM can be obtained from the equation

$$FWHM_{intrinsic}(q_{xy}) = [FWHM_{meas}(q_{xy})^2 - FWHM_{resol}(q_{xy})^2]^{1/2}. \quad (1)$$

A simple model assumes that the monolayer consists of 2-D crystallites that are perfect and have a finite average size L_{xy}, the coherence length. Using the Scherrer formula (39), we can calculate the coherence length

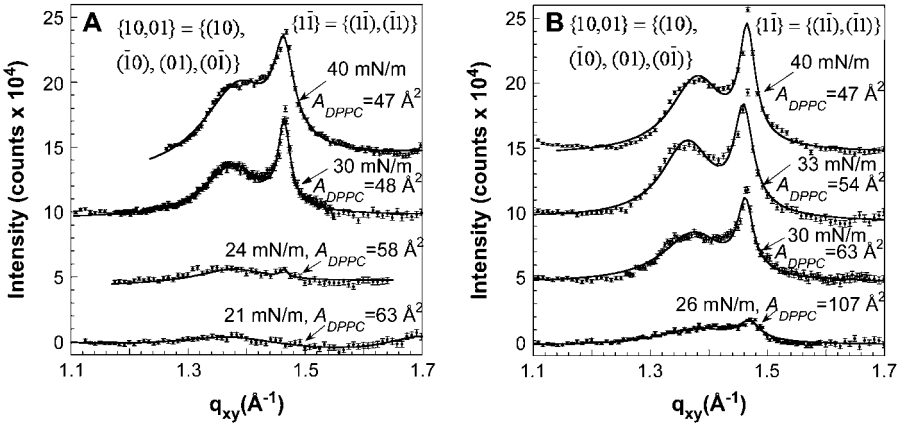

FIGURE 4 Bragg peaks from GIXD on a water subphase at 30°C for (*A*) pure DPPC and (*B*) DPPC/P188 films at various A_{DPPC}. For clarity, the data have been offset vertically. The two GIXD Bragg peaks observed for DPPC at 40 mN/m indicate a distorted hexagonal packing of the lipid tails in a 2-D unit cell with parameters $a = b = 5.05$ Å, $\gamma = 116.6°$. The Miller indices $\{h, k\}$ (distorted hexagonal lattice) are indicated for each peak. In *B*, the diffraction peak observed at $A_{DPPC} = 107$ Å^2 corresponds to a highly condensed lipid phase comparable to pure DPPC at $A_{DPPC} = 47$ Å^2, despite the large nominal A_{DPPC}. The molecular packing parameters used in the fitting are listed in Table 1.

TABLE 1 Parameters obtained from GIXD for DPPC and DPPC/P188 mixture at 30°C

			In-plane Bragg peaks			Out-of-plane Bragg rods		
Composition	π(mN/m)	Nominal A_{DPPC} (Å$_2$)	a, b (Å)	γ (°)	Area/molecule (Å^2)	Coherence length, $L_c \pm 1.0$ (Å)	Tilt direction ± 1.0°	Tilt angle $t \pm 1.0$ (°)
DPPC	30	48	5.07	116	46.1	18.9	11.9° from NN, nonsymmetry	30.0
	40	47	5.05	116	45.7	19.0	10.7° from NN, nonsymmetry	28.3
DPPC/P188	26	107	5.09	116	46.7	19.0	12.4° from NN, nonsymmetry	30.8
	30	63	5.09	116	46.7	19.0	12.2° from NN, nonsymmetry	30.0
	40	47	5.05	116	45.9	19.0	11.7° from NN, nonsymmetry	28.3

NN, nearest neighbor.

$L_{xy} \approx 0.9[2\pi/\mathrm{FWHM}_{intrinsic}(q_{xy})]$ in the two crystallographic directions $\{10,01\}$ and $\{1\bar{1}\}$, and they were found to be 54 Å and 240 Å, respectively.

The Bragg rod profiles, integrated over the q_{xy} region corresponding to the two reflections, are shown in Fig. 5 *B*. The $\{1\bar{1}\}$Bragg rod achieves its maximum intensity near $q_z \sim 0$ Å^{-1}, indicating that the molecular axis lies in a plane nearly parallel to the distortion direction of hexagonal unit cell. We analyzed the $\{10,01\}$ and $\{1\bar{1}\}$ Bragg rod intensity profiles by approximating the fatty acid tail with a cylinder of constant electron density (26). Our analysis shows that the lipid molecule has a tilt of 30.0° from the surface normal and the projected tilt direction on the water subphase is 11.9° from the nearest neighbor. The effective coherently scattering length of the DPPC molecule, L_c, is 18.9 ± 1.0 Å. The tilt direction is in a nonsymmetry direction, as in the rest of the DPPC films, which again indicates that the rectangular symmetry is broken and an oblique 2-D crystal structure was formed instead (41).

When the pure DPPC film is compressed to $A_{DPPC} = 47$ Å^2, Bragg peaks occur almost at the same positions as those at $A_{DPPC} = 48$ Å^2 (Fig. 4 *A*), and subject to experimental error, the calculated *d*-spacings are almost identical. Tilt angle of the chains from the vertical remains large (~28.3°) even at $\pi = 40$ mN/m. Previous work on DPPC has also shown large tilt angles at high lateral pressures (41,42), which can be understood via a model where the carbonyl group of the ester at the C2 position pulls the attached chain toward the water subphase (41). This suggests that the packing of DPPC molecules is mainly limited by the headgroup which maintains a large cross-sectional area at high surface pressures. After the headgroups are compressed to tight contact with each other, there remains ample space for the alkyl tails to assume large tilt angles relative to the surface

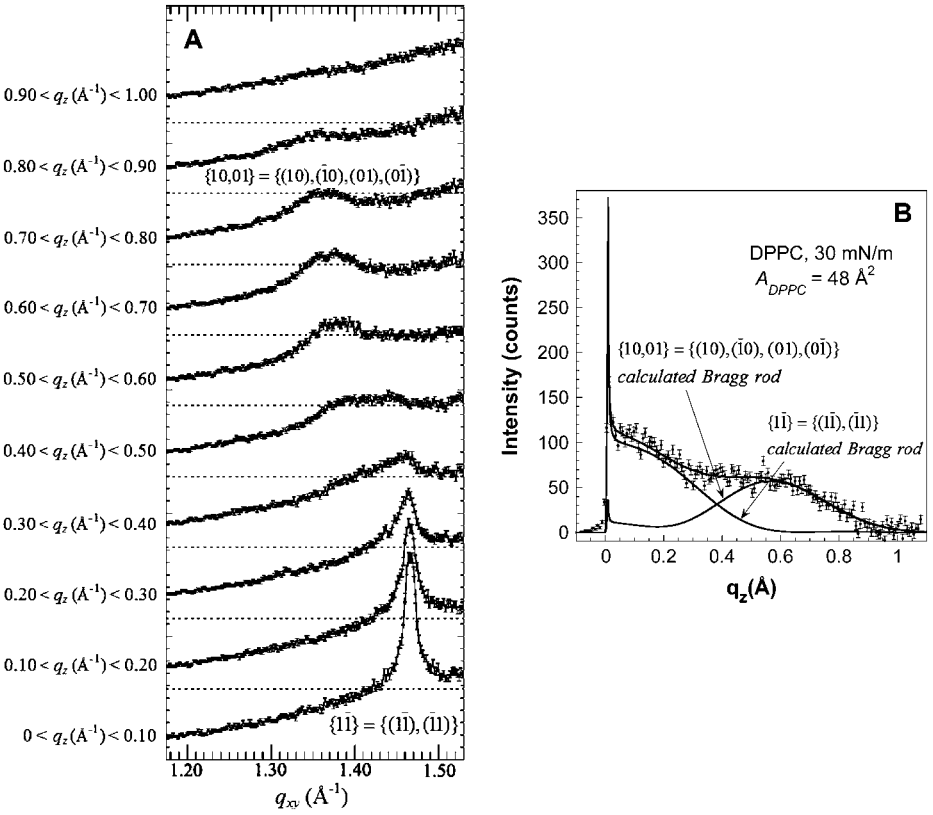

FIGURE 5 (*A*) Scattering intensity as a function of in-plane scattering vector component q_{xy} for different q_z intervals (intensity integrated over the vertical scattering vector q_z in 10 successive 0.1-Å^{-1}-wide q_z-windows, as indicated) for a pure DPPC film on a water subphase at 30°C and 30 mN/m. (*B*) Bragg rod profiles for $\{10,01\}$ and$\{1\bar{1}\}$Bragg peaks for a pure DPPC film on a water subphase at 30°C and 30 mN/m. The Bragg rods were fitted (*solid line*) by approximating the coherently scattering part of the acyl chain by a cylinder of constant electron density. The sharp peak at $q_z = 0.01$ Å^{-1} is the so-called Yoneda-Vineyard peak (Vineyard (54)), which arises from the interference between x-rays diffracted up into the Bragg rod and x-rays diffracted down and then reflected up by the interface.

normal, and the size of unit cell of the alkyl chain cannot decrease further due to the limitation of headgroup packing.

DPPC/P188 film

The Bragg peaks obtained for the P188-treated DPPC film at different surface pressures are shown in Fig. 4 *B*. Upon spreading, the nominal area for DPPC is $A_{DPPC} = 107$ Å^2. At such a large area/molecule and in the absence of P188, the DPPC film is expected to be in the gas/liquid expanded coexistence phase, with the surface pressure at 0 mN/m and with no Bragg peak present. Upon the introduction of P188 in the subphase, the surface pressure rose from 0 to 26 mN/m without any compression, and two distinct Bragg peaks are observed at $q_{xy} = 1.37$ Å^{-1} and $q_{xy} = 1.46$ Å^{-1}. The calculated *d*-spacings are 4.59 Å and 4.30 Å, which are identical to those found in Bragg peaks obtained from a pure DPPC monolayer at a much lower A_{DPPC}. The occurrence of precisely two Bragg peaks resulting from the $\{10,01\}$ and $\{1\bar{1}\}$ reflections indicates a distorted hexagonal unit cell with axes $|a| = |b| = 5.09$ Å, $\gamma = 116°$, and an interfacial area/molecule of 46.7 Å^2. Since the size of the unit cell obtained for DPPC/P188 film is almost identical to that found for pure DPPC at $A_{DPPC} = 46.1$ Å^2, coupled to the fact that pure P188 does not form ordered structure, Bragg peaks in the DPPC/188 film have to come from the DPPC crystals, and P188 does not interfere with the packing of the ordered DPPC molecules. Instead, P188 is incorporated in the disordered phase of the monolayer. The observed Bragg peaks at a large area/DPPC molecule can only be explained in one way: P188, phase-separated from DPPC, physically occupies a portion of the available surface area, and the smaller area left for the lipid forces DPPC molecules to form a condensed phase.

Fig. 6 depicts the diffracted intensity as a function of the in-plane scattering vector component q_{xy} for different q_z intervals (Fig. 6 *A*), as well as the Bragg rod profile of the DPPC/P188 film (Fig. 6 *B*). The Bragg rod results show that the chains are tilted by 30.8 ± 1.0° in a direction 12.4 ± 1.0° from the nearest neighbor, and the chain length is 19.0 ± 1.0 Å.

At $A_{DPPC} = 63$ Å^2, the Bragg peaks and Bragg rods of the P188-treated DPPC film are almost identical to those of pure DPPC monolayer at $A_{DPPC} = 48$ Å^2 (Figs. 4 *B* and 7 *A*, respectively). Two Bragg peaks resulting from $\{10,01\}$ and $\{1\bar{1}\}$ reflections are observed at $q_{xy} = 1.37$ Å^{-1} and $q_{xy} = 1.46$ Å^{-1}. The *d*-spacing values $d_{10,01} = 4.62$ Å and $d_{1\bar{1}} = 4.30$ Å indicate a distorted hexagonal unit cell with axes $|a| = |b| = 5.09$ Å, $\gamma = 116°$. Similar to the pure DPPC case, the $\{1\bar{1}\}$ Bragg rod achieves its maximum intensity at $q_z \sim 0$ Å^{-1}, and the Bragg rod profile of the $\{10,01\}$ reflection gives a tilt angle of 30.0° toward the direction of 12.2° from the nearest neighbor, with the coherently scattering length of the molecule, L_c, of 19.0±1.0 Å. Compared to pure

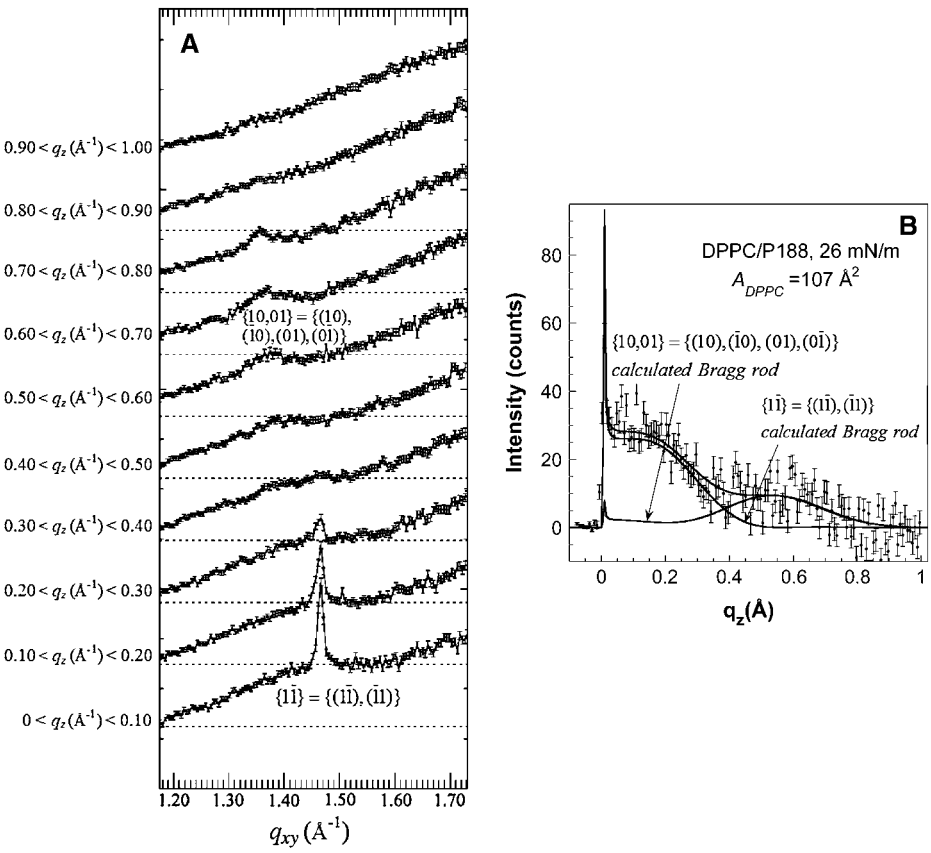

FIGURE 6 (*A*) Scattering intensity as a function of in-plane scattering vector component q_{xy} for different q_z intervals (intensity integrated over the vertical scattering vector q_z in 10 successive 0.1-Å^{-1}-wide q_z-windows, as indicated) for the P188-treated DPPC film on a water subphase at 107 Å^2/DPPC molecule and 30°C. (*B*) Background subtracted Bragg rod intensity distribution along q_z vector integrated over the q_{xy} range of the Bragg peaks. The rod was fitted (*solid line*) by approximating the coherently scattering part of the DPPC tail by a cylinder of a constant electron density.

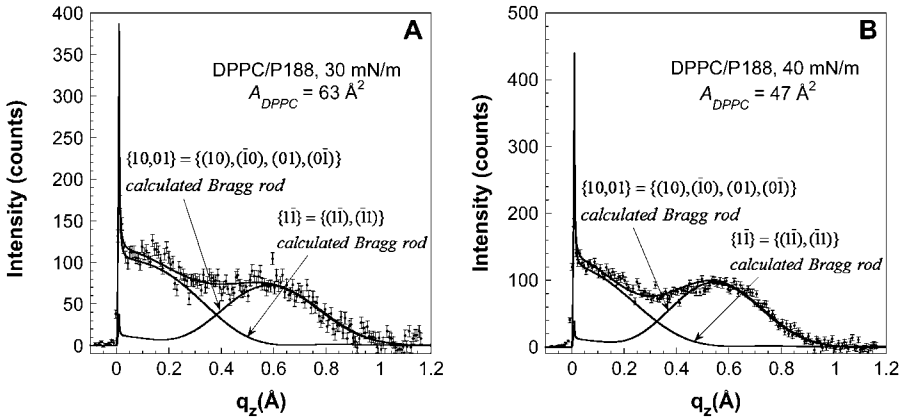

FIGURE 7 Bragg rod profiles for Bragg rods in the $\{10,01\}$ and $\{1\bar{1}\}$ directions for a DPPC/P188 film on a water subphase at (*A*) A_{DPPC} = 63 Å^2 and (*B*) A_{DPPC} = 47 Å^2, both at 30°C. The rods were fitted (*solid line*) by approximating the coherently scattering part of the alkyl chain by a cylinder of constant electron density.

DPPC, these results again confirmed that P188 does not affect the lipid packing of the condensed phase. The unit cell and the molecular tilt found in the condensed phase of DPPC are preserved in this mixed system, suggesting that P188 is completely excluded from the condensed region of the film.

For our particular scan, the integrated intensity observed for the Bragg peaks of DPPC/P188 film at $A_{DPPC} = 107$ Å^2 is ~12% of that at $A_{DPPC} = 47$ Å^2. According to fluorescence microscopy (22), at $A_{DPPC} = 47$ Å^2, the DPPC/P188 film is mainly composed of condensed phase. Because GIXD is sensitive only to the ordered phase, this decrease in scattering intensity suggests that an ordered phase in DPPC/P188 film at $A_{DPPC} = 107$ Å^2 occupies ~12% relative to that at $A_{DPPC} = 47$ Å^2. It should be noted that the area coverage reported here for DPPC only reflects the distribution of the portion of the film scanned by the x-ray beam; the actual number could fluctuate depending on the heterogeneity of the film. Nonetheless, at $A_{DPPC} = 107$ Å^2 there is a substantial increase in the area occupied by the condensed DPPC domains in the presence (~12%) of P188 compared to the absence (0%) of P188.

For the DPPC/ P188 monolayer, at $A_{DPPC} = 47$ Å^2 (Figs. 4 *B* and 7 *B*), the integrated intensities observed with and without P188 are the same, indicating that both films have a similar amount of ordered phase. The in-plane coherence lengths of DPPC crystallites in pure DPPC and DPPC/P188 films at $A_{DPPC} = 47$ Å^2 are also almost identical ($L_{10,01} \sim 40$ Å, $L_{1\bar{1}} \sim 200$ Å). This suggests that at low area/molecule (or high lipid density), P188 no longer stays in the lipid film. This finding corroborates our isotherm data indicating that at high surface pressures ($\pi > 36$ mN/m), the phase behavior of the DPPC/P188 system reverts back to the pure DPPC.

DPPG and DPPG/P188

Similar phenomena related to tightening the packing of the lipid molecules have also been observed for DPPG. When the area/DPPG molecule (A_{DPPG}) is 84 Å^2, pure DPPG monolayer is in the liquid-expanded phase, and no Bragg peak is observed (see Fig. 8 *A*). With P188 in the subphase at the same nominal $A_{DPPG} = 84$ Å^2, one $\{1, 0\}$ in-plane Bragg peak (in our notation, $\{1,0\}$ indicates six coinciding reflections $\{h,k\}=\{(1,0), (0,1), (\bar{1},1), (\bar{1},0), (0,\bar{1}), (1,\bar{1})\}$) is observed at $q_{xy} = 1.49$ Å^{-1} (Fig. 8 *B*), indicating the existence of 2-D crystallites with a hexagonal unit cell: $a = b = 4.83$ Å, $\gamma = 120°$, and $A = 20.2$ Å^2 per tail. Comparing this Bragg peak with that of pure DPPG at $A_{DPPG} = 39$ Å^2 (Fig. 8 *A*, Table 2), the dimensions of this unit cell of DPPG/P188 film at $A_{DPPG} = 84$ Å^2 are almost identical to those of the

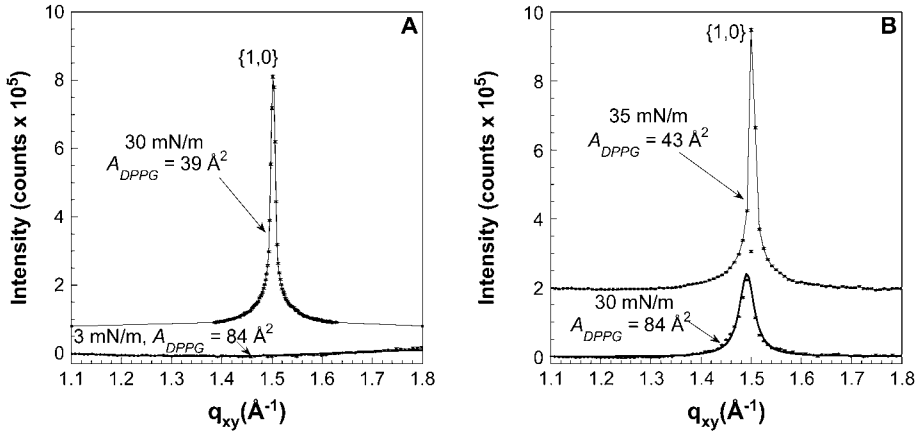

FIGURE 8 Bragg peaks at different packing densities from GIXD on a water subphase at 30°C of (*A*) pure DPPG and (*B*) DPPG/P188 films. For clarity, the data have been offset vertically.

TABLE 2 Parameters obtained from GIXD for DPPG and DPPG/P188 film at 30°C

			In-plane Bragg peaks				Out-of-plane Bragg rods		
Composition	π(mN/m)	Nominal area/ molecule (Å^2)	Unit cell	a_H (Å)	$A = 2ab$ sinγ (Å^2)	$L_{10,01,1\bar{1}}$ ±25 (Å)	L_c ± 0.5 (Å)	Tilt direction	Tilt angle ± 0.9°
DPPG	3	84				No peak			
	30	39	Hexagonal	4.83	40.4	670	18.9	Nearest neighbor	5.1°
	35	37	$a_H = b_H, \gamma = 120°$	4.82	40.2	850	18.5	Nearest neighbor	2.4°
DPPG/P188	30	84	Hexagonal	4.86	40.8	220	18.9	Nearest neighbor	9.4°
	35	43	$a_H = b_H, \gamma = 120°$	4.83	40.4	380	19.0	Nearest neighbor	5.5°

pure DPPG monolayer at $A_{DPPG} = 39$ Å^2, again demonstrating that P188 does not interfere with the packing of ordered lipid molecules. Similarly, identical lattice parameters for DPPG are obtained in the absence and presence of P188 at even lower A_{DPPG} (see Table 2).

A finite size of the crystalline domain leads to the broadening of Bragg peaks. The coherence lengths L_{xy} calculated from the FWHM of Bragg peaks are listed in Table 2, along with the orientation of these straight alkyl chains (chain length L_c, tilt direction, and tilt angle). There is a pronounced decrease in the coherence length L_{xy} of the DPPG/P188 film compared to that of pure DPPG. Comparing the intensities of Bragg peaks at 30 mN/m, the intensity of the DPPG/P188 peak is 66.4% of that of pure DPPG; this is due to the presence of P188 in the footprint and smaller coherence length of crystallites in the DPPG/P188 film.

X-ray reflectivity

Pure DPPC

XR measurements were carried out for both DPPC (Fig. 9) and P188-pretreated DPPC monolayers below and above the ''squeeze-out pressure'', the surface pressure beyond which isotherms of pure DPPC and P188/DPPC superimpose. The pure lipid monolayers were fitted with the simplest two-box model (see Table 3, Fig. 9): one for the headgroup region and one for the tail region, with only one root-mean-square (roughness) parameter to smear out the interfaces. During the refinement and model fitting the number of electrons in the tail region was fixed to 242 (value calculated from the chemical formula for DPPC) and the area/molecule was fixed to the measured value to reduce the number of fitting parameters.

For DPPC at 21 mN/m, the fit gives a hydrocarbon layer thickness of 12.3 ± 0.3 Å, resulting in a molecular tilt of 49 ± 2° and a total film thickness of 20.9 Å. At 24, 30, and 40 mN/m, the thickness of the hydrocarbon layer increases to 13.0 ± 0.2 Å, 15.7 ± 0.2 Å and 16.1 ± 0.3 Å, respectively, since the tails are less tilted at higher lipid packing densities (with tilt angles of 46 ± 2°, 34 ± 2°, and 31 ± 2°, respectively). Comparing the XR results of DPPC at 30 mN/m to GIXD measurements, the tilt angles from XR are larger. This is due to the fact that XR measurements, unlike GIXD, are sensitive to both the crystalline and noncrystalline phases, with molecules in the latter having larger tilt angles as they are more loosely packed. The number of electrons in the headgroup region decreases inversely with surface pressure (due to the elimination of hydrating water molecules from the headgroup region upon tight packing), whereas the electron densities of both the headgroup and the alkyl tail increase with compression, as expected.

The lipid headgroups of monolayers are of particular interest, since they constitute the interaction sites with the aqueous environment and peripheral membrane proteins (43). For a pure DPPC monolayer, noting that the bare PC headgroup has 164 electrons, the extra electrons associated with the headgroup could only be attributed to the hydrating

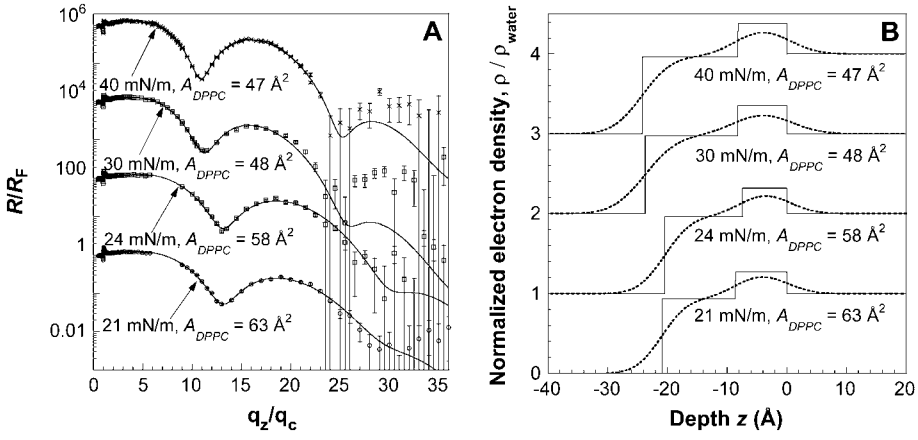

FIGURE 9 (*A*) X-ray reflectivity data for a DPPC monolayer on a water subphase at various surface packing densities at 30°C. The solid lines are fits to the data using box models, as discussed in the text. (*B*) The corresponding normalized electron density profiles for XR data. For clarity, the data have been offset vertically for all panels. $z = 0$ signifies the start of the water subphase. The fitting parameters are listed in Table 3.

TABLE 3 Fitting parameters for XR data of DPPC on pure water at 30°C

	Headgroup region				Tail region				
π(mN/m)	Thickness(Å)	ρ/ρ_{H2O}*(No. of e^-)	N_{water}	$V_{o,head}$(Å^3)	Thickness(Å)	ρ/ρ_{H2O}*(No. of e^-)	σ(Å)	χ^2	Area/molecule(Å^2)
21	8.6 ± 0.5	1.27 ± 0.12 (229 ± 5)	6.5	346	12.3 ± 0.2	0.94 ± 0.02 (242†)	3.41 ± 0.04	7.84	63†
24	7.4 ± 0.6	1.32 ± 0.18 (189 ± 6)	2.5	354	13.0 ± 0.2	0.96 ± 0.02 (242†)	3.54 ± 0.04	10.0	58†
30	8.2 ± 0.4	1.35 ± 0.10 (178 ± 4)	1.4	351	15.7 ± 0.2	0.96 ± 0.02 (242†)	4.27 ± 0.03	4.86	48†
40	8.2 ± 0.3	1.38 ± 0.04 (178 ± 5)	1.4	343	16.1 ± 0.3	0.96 ± 0.02 (242†)	3.88 ± 0.01	6.23	47†

*All electron densities are normalized by the electron density of water, $\rho_{water} = 0.334e^-/\text{Å}^3$, and are reported with three significant figures. σ is the root mean square roughness of the interface.
†Parameter was fixed during refinement.

water molecules. The number of water molecules in the hydration shell of each headgroup (N_{water}) is listed in Table 3. From the fitted thickness of the headgroup box, as well as the area/molecule from the isotherm, the total volume of the headgroup region is known. If it is assumed that the partial volumes are additive, then the bare headgroup volume ($V_{o,head}$) can be calculated, and the value is listed in Table 3. For the component volume of each water molecule, the bulk value $V_w = 30.0$ Å^3 has been used. It is worth noting that the calculated bare headgroup volumes from different surface pressures turn out to be almost constant, and agree well with reported values (44,45), within the error range of a few Å^3.

We further note that M. Schalke analyzed reflectivity data for DPPC at 22°C (46), accounting for the lipid headgroup in terms of its three components (glycerol backbone, phosphate, and choline) described by partly overlapping volume-restricted distribution functions along the z axis (43,47). With additional information from FTIR and neutron reflectivity, a similar pressure dependence of headgroup hydration has been found.

DPPC/P188

$\pi = 26\,\text{mN/m}$, precompression at $A_{DPPC} = 107$ Å^2

Strong corroborative evidence for phase separation of P188 from DPPC molecules can be found from the heterogeneity of the DPPC/P188 film observed with XR. For DPPC/P188 on pure water at $A_{DPPC} = 107$ Å^2 and 30°C, scanning different regions results in significantly different reflectivity profiles. The analysis shows that one region is mainly composed of P188 (Fig. 10 *A*), and the other is mainly composed of DPPC condensed-phase domains (Fig. 10 *B*). In Fig. 10 *A*, the XR curve shows no interference in the measured q_z range and is very similar to those of pure P188 (Fig. 3), indicating that this region of the film is primarily composed of P188 that has a very low contrast in electron density compared to water. The data can be fitted with a one-box model for P188 at the interface, and the fitting results give a film thickness of 29.9 ± 1.4 Å, with an electron density 1.07 ± 0.01 times that of water. The mixed DPPC/P188 film has a larger thickness and an electron density comparable to that of pure P188 before compression (21.6 ± 1.0 Å, with electron density 1.04 ± 0.01 times that of water). This is possibly due to the presence of a DPPC molecule arranging in a staggering manner with P188 and thereby enhancing the overall average thickness of the surface layer. Alternatively, P188 in the presence of DPPC may exist in a more extended conformation compared to pure P188.

In Fig. 10 *B*, the XR curve shows the typical features of a layered structure, and can be fitted with a two-box model, one for the DPPC tail/P188 region and the other for the headgroup/P188 region. Since the electron density contrast between P188 and water is very small, a layer of P188 underneath the DPPC headgroup region is difficult to detect by XR, although it is likely that such a layer exists. Once again, the electron density contrast between P188 and the

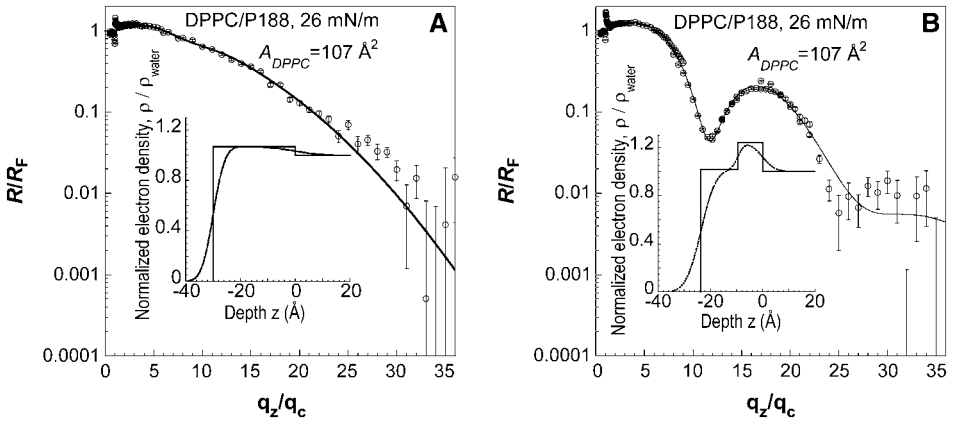

FIGURE 10 X-ray reflectivity data and fit for a DPPC/P188 film at (*A*) the P188-rich portion and (*B*) the DPPC-rich portion. The insets are the corresponding normalized electron density profile $\rho(z)/\rho_{water}$ in smeared (by interfacial roughness) and unsmeared forms. $z = 0$ signifies the start of the water subphase. The fitting parameters are listed in Table 4.

alkyl tail is small, whereas the contrast between P188 and the DPPC headgroup is significant. The existence of P188 in the DPPC layer can therefore be confirmed by the reduction of the electron density for the headgroup region of pure DPPC at a similar surface pressure.

The fit results for the mixed system are presented in Table 4. Results presented here are obtained by using the simplest possible model. We can fit the high q_z range more precisely by including more parameters (e.g., different roughness on different interfaces). We have attempted such fittings with higher precision, but they do not give us any new information as far as the electron density and the box thickness are concerned.

When the x-ray beam falls within either region, a normal XR curve is obtained, as shown in Fig. 10. However, when the x-ray beam crosses the boundary of the two regions, poor overlaps in the reflectivity curve were observed (data not shown) when part of the q_z range was remeasured before and after beam translation. Poor overlaps have been observed when the beam was moved from a P188-rich region (similar to Fig. 10 *A*) to a lipid-rich region (similar to Fig. 10 *B*), as well as in the opposite direction. Since changes in both directions have been observed, beam damage can be excluded as the potential cause for such poor overlaps, as it only alters the intrinsic feature of the XR curve to that of a bare water interface but can never induce lipid features, as observed in half of our cases showing poor overlaps. Furthermore, XR data measured on the same surface positions are reproducible.

Our analysis suggests that P188 inserts all the way to the end of the DPPC tail group. Despite attempts to divide the tail region into two boxes, least-square fitting always reverts back to parameters corresponding to only one box for the tail region. Although the electron density contrast between DPPC tail and poloxamer is low, neutron reflectivity experiments with specific site deuteration to afford better contrast are currently underway to elucidate the extent of poloxamer insertion into the tail region.

$\pi = 33\,\mathrm{mN/m}$

At 33mN/m the film remains heterogeneous, giving either lipid-rich or lipid-poor featured XR curves (see Table 4) depending on the location of the x-ray beam. To illustrate surface hererogeneity, two XR curves (not shown here but similar to Fig. 10 *B*) representing the two regions of the film were collected and analyzed. Similar to the case of 26 mN/m, the fitting parameters calculated from P188 surface coverage, which is estimated from the expansion of A_{DPPC} in DPPC/P188 film compared to that of pure DPPC, serve as good starting points for fitting these XR data, and the resulting fitting parameters are listed in Table 4. Results from fitting indicate that the P188 content corresponds to 15% and 29%, respectively.

$\pi = 40\,\mathrm{mN/m}$

The XR data for both pure DPPC and DPPC/P188 films are shown in Fig. 11 *A*. Both the XR curve and the corresponding electron density profile of the DPPC/P188 film are identical to those of pure DPPC. These data corroborate the theory that at high surface pressures, P188 is squeezed out from the DPPC monolayer, as indicated earlier by our isotherm results. With the exclusion of P188 from the monolayer, the thickness of the former DPPC headgroup/P188 region also decreases and reverts back to the value of pure DPPC. It should be noted that for all measurements taken at this surface pressure, the results are independent of the location of the footprint of the x-ray beam. This is in contrast to observations obtained at higher areas/molecule (lower surface pressures) when P188 is present.

DPPG and P188-DPPG

We have also carried out similar XR experiments for DPPG and DPPG/P188 films (data not shown), and have obtained

TABLE 4 Fitting parameters for XR data of DPPC/P188 on pure water at 30°C¶

		DPPC headgroup/P188 region		Tail/P188 region				
π(mN/m)	Portion of film	Thickness (Å)	ρ/ρ_{H2O}* (No. of e^-)	Thickness (Å)	ρ/ρ_{H2O}* (No. of e^-)	$\sigma^{\dagger}$(Å)	χ^2	Area/ molecule(Å^2)
26	P188-rich	Thickness = 29.9 ± 1.4; ρ/ρ_{H2O} = 1.07 ± 0.01 (one box)				5.5 ± 1.8‡	3.03	107§
	DPPC-rich	9.4 ± 1.0	1.24 ± 0.02 (417 ± 7)	14.2 ± 0.7	1.02 ± 0.04 (518 ± 20)	3.4 ± 0.6‡	13.2	107§
33	P188-rich	7.6 ± 0.8	1.28 ± 0.03 (179 ± 19)	14.8 ± 0.6	0.98 ± 0.04 (266 ± 11)	4.1 ± 0.6‡	9.97	55§
	DPPC-rich	8.4 ± 1.1	1.33 ± 0.02 (205 ± 21)	15.8 ± 0.6	0.97 ± 0.02 (283 ± 14)	3.8 ± 0.1	2.63	55§
40	DPPC	8.2 ± 0.3	1.38 ± 0.03 (178 ± 4)	16.0 ± 0.2	0.96 ± 0.02 (242 ± 3)	3.9 ± 0.1	17.0	47§

*All electron densities are normalized by the electron density of water, $\rho_{\mathrm{water}} = 0.334e^-/\mathrm{Å}^3$, and are reported with three significant figures.

$^{\dagger}\sigma$ Root-mean-square roughness of the interface.

‡Average of three roughness values for the two-box model.

§Parameter was fixed during refinement.

¶At surface pressures below squeeze-out pressure, our fluorescence microscopy study revealed that the DPPC-rich regions and P188-rich regions can be as large as ~15 mm in width. Although fluorescence microscopy does not provide information at the submicron meter length scale, atomic force microscopy results on DPPC/P188 film deposited on a solid substrate show that each region is actually composed of nanoscale domains. This length scale is smaller than the coherence length of the x-ray beam (micrometers × hundreds of Ångströms (26,29)). Beyond the squeeze-out pressure, only lipid molecules in the condensed phase remain at the surface, leaving a homogenous film. Hence we can treat our XR data with coherent averaging (34).

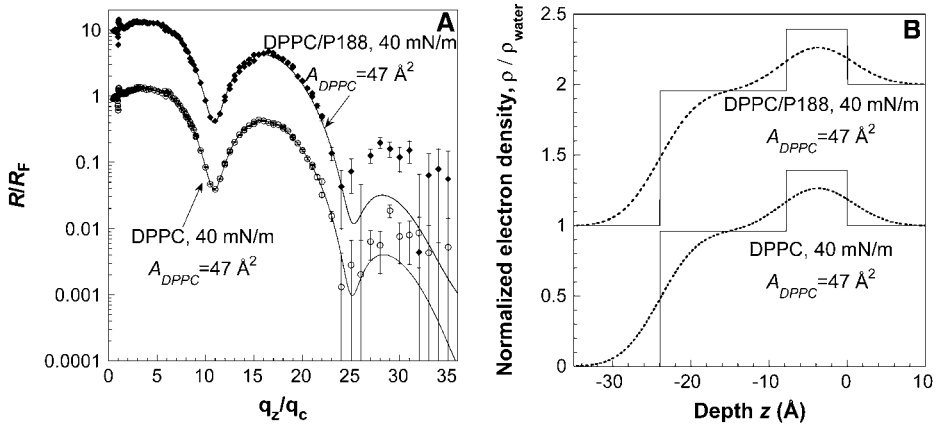

FIGURE 11 (*A*) X-ray reflectivity data for DPPC and DPPC/P188 films on a water subphase at $A_{\mathrm{DPPC}} = 47$ Å^2. The solid lines are fits to the data using the box models discussed in the text. (*B*) The corresponding normalized electron density profiles for the XR data. $z = 0$ signifies the start of the water subphase. For clarity, the data have been offset vertically. The fitting parameters are listed in Table 4.

similar results as in the DPPC case. At low surface pressures ($\pi < 38$ mN/m) P188 remains inserted into the DPPG monolayer. The presence of the poloxamer results in similar surface heterogeneities to those observed for DPPC, giving rise to DPPG-rich and P188-rich regions in the surface film. Such heterogeneities are reflected by the different XR profiles observed at a given surface pressure (data not shown). At high surface pressure ($\pi > 38$ mN/m), P188 is squeezed out from the tail portion of DPPG monolayer. Although DPPC and DPPG have different headgroup charges, our observation shows that P188 insertion is not influenced by electrostatics. This should not be surprising, as P188 is a nonionic surfactant.

DISCUSSION

Our isotherm results demonstrate that P188 is a highly surface-active copolymer. With the presence of a lipid film at the air-water interface at 0 mN/m and 30°C, the injection of P188 into the subphase at a final concentration of 50 μM reduces the surface tension and increases the surface pressure from 0 to 26 mN/m in 40 min. The surface pressure changes sharply in the first few minutes after P188 injection; after 10 min, the change becomes gradual and slow. After 40 min, XR scans on P188 over time (with a 2-h gap) show small differences that are within the error range (data not shown). All x-ray scattering data presented here were taken at least 40 min after helium flushing, at which point the adsorption of P188 to the air-water interface is so slow that any residual change in the film structure over time can hardly be detected by XR. It is likely that the slow P188 adsorption into lipid monolayer slightly changes the occupancy of lipid-rich regions. Besides, there might also be a conformational change of P188 at the interface.

XR and GIXD measurements have been used to provide molecular-level information for the insertion of P188 into the DPPC and DPPG monolayers at the air-water interface. They both agree well with the postulate that P188 interacts with structurally disrupted membrane portions, and is effectively excluded from the once-damaged portion when the lipid packing density of a normal membrane has been reestablished. Recently, the squeezing-out of Gemini surfactants with anti-HIV activity from the phospholipid monolayer upon compression has also been reported (48).

It is clear from our GIXD data that P188 does not affect the molecular packing of the ordered phase of DPPC, suggesting that P188 is completely excluded from the ordered portion of the monolayer. Our findings also indicate that P188 and DPPC do not mix well with each other. Such demixing has been observed to occur almost instantaneously upon P188 adsorption to the lipid film via fluorescence microscopy (data not shown). Clear evidence of phase separation between P188 and the ordered lipid phase is provided by GIXD measurements taken ~40 min after the introduction of the poloxamer.

The presence of P188 at the interface acts to force lipid molecules to pack more tightly, and the amount of P188 incorporated into the DPPC film is likely to be controlled by the surface free energy. When the surface pressure of DPPC monolayer is low (<36 mN/m), P188 adsorbs to the air-water interface and physically occupies a portion of the available area, causing the subsequent formation of 2-D crystallites of DPPC molecules. When the surface pressure is increased to >36 mN/m, the close contact between P188 and DPPC becomes unfavorable and P188 is entirely squeezed out from the DPPC tail region. In the context of membrane sealing, the insertion of poloxamer into a low-density lipid film at the air/water interface helps elucidate the mechanism by which the poloxamer seals damaged membranes in living cells. In effect, the low-density lipid film in our model system mimics the hydrophobic-aqueous environment found both at the highly curved lipid portion that constitutes the pore on a damaged membrane, and in the portion of the membrane that has enhanced permeability due to a reduction in lipid density. Just as in our model system, both of these sites in a damaged membrane have an enhanced exposure of the lipid hydrocarbon tail to the aqueous environment, into which the poloxamer inserts. Such an insertion results in the

tightening of the lipid packing, as demonstrated in our GIXD results. This, along with the fact that the PEO portion of the polymer remains situated in the aqueous phase with a certain radius of gyration, helps restore the barrier function of the damaged membrane and reduces its permeability. Even when a pore exists on the membrane surface, we do not expect the poloxamer's sealing action to be brought about by its insertion into the water-water interface. Rather, by inserting into the highly curved regions around the pore, the poloxamer can help bring lipids on different sides of the pore together and displace water molecules out of the pore region, thus eliminating the pore formation and restoring the barrier function.

Phase separation in lipid/poloxamer systems has previously been inferred (49). Differential scanning calorimetry (DSC) has shown that the liposomal bilayer's main phase transition endotherm broadens with a shoulder at high poloxamer concentration, indicating the presence of two distinct entities. Moreover, the decrease in mean liposome radius implies the possible existence of mixed micelles. Nonetheless the DSC and size analysis results only indirectly point to a separation between poloxamer-rich and poloxamer-poor phases. DPPC ordering by P188 and the surface inhomogeneity observed here unambiguously confirm such phase separation. In the context of membrane sealing, P188 insertion increases the lipid packing density, which in turn helps arrest leakage, as observed in damaged cells (2,50). Although the presence of P188 would increase the lipid packing density, we do not expect the lipids to attain the gel state in real membranes due to the large fraction of unsaturated lipids present.

The incapability of P188 to remain in the system at high surface pressures can be beneficial in terms of its application as a membrane sealant. After electroporation, cells may activate a self-healing process, restoring the structural integrity of the lipid bilayer of the cell membrane. As the cell heals and the lipid packing of the membrane is restored, our data suggests that there is a mechanism through which P188 exits the membrane.

The selective insertion of P188 into low- over high-density lipid film helps to clarify some of the earlier findings on the interaction between poloxamers and different lipid bilayers. It has been suggested (51) that poloxamers associate with relatively fluid eggPC bilayers, resulting in an increased particle size caused by the projection of PEO groups from the liposome surface. This was not observed when poloxamers were added to gel state DSPC liposomes (52). It has also been found by DSC (49) that phospholipid bilayer pretransition enthalpy was reduced when poloxamers interacted with the liquid-crystalline state, but not gel-state liposomes. These findings can now be understood in terms of lipid ordering tuning poloxamer insertion, where loose packing in the fluid bilayer promotes insertion whereas tight packing in the gel state inhibits insertion. Moreover, our data suggest that poloxamer interacts with liposomes via penetration into liquid crystalline state bilayers rather than adsorption onto liposome surfaces. Previous work has also reported similar results for peptide-lipid interactions with monolayer and bilayer models (53). Although our monolayer work can help shed light on bilayer studies, differences may exist in the conformation and orientation of the interacting poloxamer.

APPENDIX A

Surface heterogeneity of DPPC/P188 film at A_{DPPC} = 107 Å^2

At large nominal area DPPC ($A_{\mathrm{DPPC}} = 107$ Å^2, $\pi = 26$ mN/m), we have performed fluorescence microscopy measurements, and have found that the adsorption of poloxamer at the air/water interface blackens out the monolayer initially in gas (dark)/liquid-expanded (bright) coexistence (see Fig. 12), and cuts the surface into regions with different gray levels (Fig. 13). These regions can be of the length scale of $\sim$ 15 mm.

At intermediate surface pressures (e.g., $A_{\mathrm{DPPC}} = 55$ Å^2, $\pi = 33$ mN/m), similar surface heterogeneities have been observed. Fluorescence microscopy results suggest that the DPPC-rich and DPPC-poor regions can be as large as $\sim$ 15 mm in width. To complete one XR measurement, the sample stage is usually translated by 6 mm. Depending on the starting location of the x-ray footprint, there are variations in the distance the beam needs to be moved to locate the reported changes in the XR curves. To ensure that the observed heterogeneity is real, we have repeated the experiment on more than eight fresh samples of the DPPC/P188 system at $A_{\mathrm{DPPC}} = 110$ Å^2 ($\pi = 26$ mN/m). For each sample, we have carried out multiple XR scans either by translating the beam or by staying at the same spot and measuring over time. Observations from these experiments confirm the existence of surface heterogeneities at this pressure. Similar systems of DPPC with other poloxamers of different molecular weight and hydrophobicity (not descirbed in this manuscript) have also been studied, and similar heterogeneous XR curves have been observed for every film.

In our experiments, we use the entire trough (approximately tens of cm) to model the packing around the damaged portion of the membrane (approximately submicron meter), therefore the length scale of poloxamer patches observed in our experiments are not representative of that found in a damaged membrane. We observe approximately millimeter poloxamer-rich patchts inserted at the surface when the starting lipid packing density is low. The existence of these large length scale patches is due to the fact that the initial lipid packing density is less than half of that expected for an intact membrane, and thus the poloxamer occupied 50% of the surface area upon

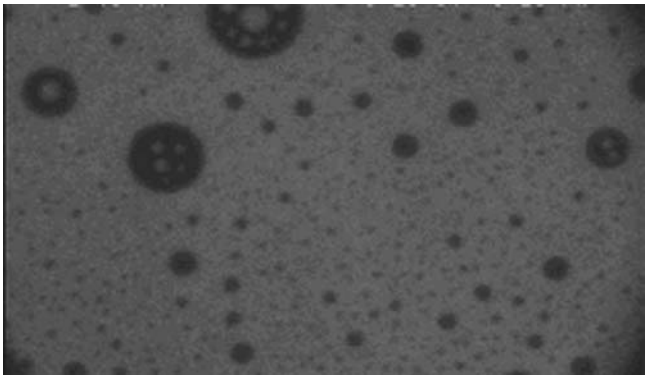

FIGURE 12 Fluorescence micrograph of a DPPC monolayer at $A_{\mathrm{DPPC}} =$ 110 Å^2, showing the coexistence of gas (dark) and liquid-expanded (bright) phases. The width of the micrograph is 550 mm.

FIGURE 13 Fluorescence micrographs after P188 injection at a nominal area of $A_{DPPC} = 110$ Å^2. (*A*) dark-gray (DPPC-rich); (*B*) one example showing coexistence of dark and light gray; (*C*) light gray (DPPC poor). The width of each micrograph is 550 mm.

insertion for $A_{DPPC} = 107$ Å^2 (the coverage of inserted poloxamer decreases as the degree of integrity loss decreases). Although the surface occupancy of the poloxamer in our model system should reflect that found in the damaged membrane of the cell, the physical length scale of the poloxamer patches does not have any bearing on the actual system.

APPENDIX B

Monitoring the beam damage

In the XR measurements of DPPC/P188 films at relatively low surface pressures, we have obtained different XR data when we move the footprint of the x-ray beam to different regions of the film. Beam damage could be a plausible cause for the observed behavior. To verify that the observed differences of the XR profiles were not caused by beam damage, we have measured XR as a function of time without moving the x-ray beam. If beam damage was indeed the culprit, identical result could not be achievable. Fig. 14 shows that two XR curves taken 2 h apart. Close examination indicates that the two curves are basically identical up to $q_z/q_c = 25$. Since the intensity minima at $q_z/q_c \approx 10$ greatly deviate from the Fresnel curve, they constitute the most sensitive location to reflect possible beam damages. The fact that these minima are identical excludes the possibility that there is any beam damage in the two curves taken 2 h apart.

The slight difference observed here can be due to a time effect intrinsic to the system. The fitting results show that the parameters for the thickness and electron density are identical for the two cases with only the roughness for the interfaces being different. (For the first measurement, the roughness is 3.87 Å, and after 2 h it increases to ~4.76 Å.) As discussed earlier, the P188 is squeezed out from the DPPC film upon compression. One possible explanation for the increase in roughness with time is that P188, upon squeeze-out (where the relatively hydrophobic PPO portion becomes excluded from the alkyl chain region), rearranges under the headgroup and undergoes conformational changes with time.

APPENDIX C

All initial pressures reported in this study are ~4 mN/m higher than in our previous published results (22). This is due to the fact that the pressures were recorded 5 min after P188 injection in previous experiments (22), whereas data reported here were taken 40 min after injection to match the waiting time needed in x-ray experiments for He flushing. A similar difference is also found in the squeeze-out pressure reported below.

APPENDIX D

The distorted-hexagonal lattice ($a = b$, $\gamma \neq 120°$) can be thought of as arising through the distortion of a hexagonal lattice in a symmetry direction. It can also be described as a centered rectangular lattice (40): $a_r = 2a\cos(\gamma/2), b_r = 2a\sin(\gamma/2)$, and $\gamma_r = 90°$. If a hexagonal lattice is distorted in a nonsymmetry direction, an oblique lattice results.

APPENDIX E

Three Bragg peaks were observed by Brezesinski et al. (41) for DPPC at 30 mN/m, but at 15°C, $q_{xy} = 1.351$, 1.382, and 1.459 Å^{-1} indicating an oblique lattice, albeit with two peaks at $q_{xy} = 1.351$, 1.382 Å^{-1} barely resolved. Also, the tilt direction was deduced to be in a nonsymmetry direction, again indicating that the centered-rectangular symmetry was broken.

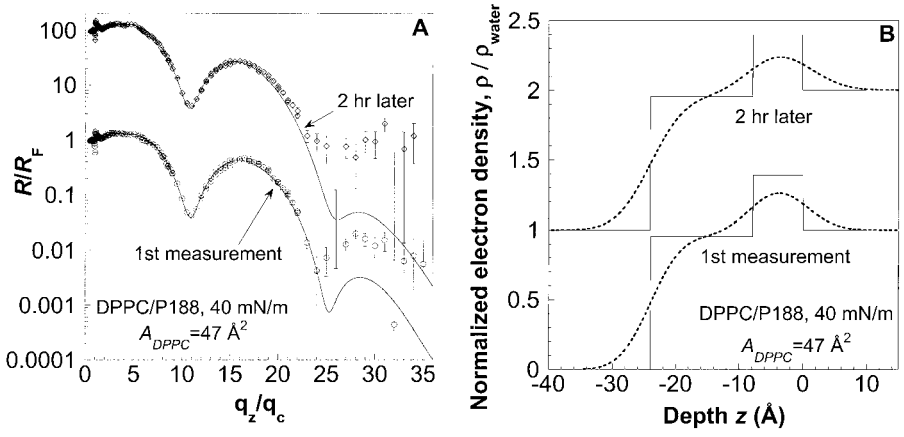

FIGURE 14 (*A*) X-ray reflectivity data for a DPPC/P188 film on a water subphase at 40 mN/m with time elapse of 2 h in between. The solid lines are fits to the data using box models discussed in the text. (*B*) The corresponding normalized electron density profiles for XR data. $z = 0$ signifies the start of water subphase. For clarity, the data have been offset vertically.

The authors thank Dr. Raphael C. Lee for helpful discussions on the subject of poloxamers as membrane sealants, and Dr. Josh Kurutz for help with the manuscript. We gratefully acknowledge beamtime on the BW1 undulator beamline at Hamburger Synchrotronstrahlungslabor (HASYLAB) at Deutsches Elektronen Synchrotron, Hamburg, Germany.

Financial support for the BW1 diffractometer and for M.W. under the DanSync Program of the Danish Natural Science Research Council is appreciated. G.W. acknowledges the support of Burroughs Wellcome Fund Interfaces No. 1001774. J.M. was supported by Los Alamos National Laboratory under Department of Energy contract W7405-ENG-36, and by the Department of Energy Office of Basic Energy Sciences. C.E was supported by the Alzheimer's Association (IIRG-9901175), American Health Association foundation (A-1999057), and the University of Chicago Materials Research Science and Engineering Centers Program of the National Science Foundation under Award DMR0213745. K.Y.C.L. is grateful for support from the David and Lucile Packard Foundation (99-1465), the Henry and Camille Dreyfus Foundation (NF-98-048), and the Alfred P. Sloan Foundation (BR-4028). The experimental apparatus was made possible by a National Science Foundation Chemistry Research Instrumentation and Facilities/Junior Faculty Grant (CHE-9816513).

REFERENCES

1. Lee, R. C., and M. S. Kolodney. 1987. Electrical injury mechanisms: electrical breakdown of cell membranes. *Plast. Reconstr. Surg.* 80: 672–679.
2. Lee, R. C., L. P. River, F.-S. Pan, L. Ji, and R. L. Wollmann. 1992. Surfactant-induced sealing of electropermeabilized skeletal muscle membranes in vivo. *Proc. Natl. Acad. Sci. USA.* 89:4524–4528.
3. Lee, R. C., D. C. Gaylor, D. Bhatt, and D. A. Israel. 1988. Role of cell membrane rupture in the pathogenesis of electrical trauma. *J. Surg. Res.* 44:709–719.
4. Lee, R. C., and M. S. Kolodney. 1987. Electrical injury mechanisms: dynamics of the thermal response. *Plast. Reconstr. Surg.* 80:663–671.
5. Lee, R. C., D. Zhang, and J. Hannig. 2000. Biophysical injury mechanisms in electrical shock trauma. *Annu. Rev. Biomed. Eng.* 02:477–509.
6. Weaver, J. C., and Y. A. Chizmadzhev. 1996. The theory of electroporation: a review. *Bioelectrochem. Bioenerg.* 41:135–160.
7. Lee, R. C., J. N. Aarsvold, W. Chen, R. D. Astumian, M. Capelli-Schellpfeffer, K. M. Kelley, and N. H. Pliskin. 1995. Biophysical mechanisms of cell membrane damage in electrical shock. *Semin. Neurol.* 15:367–374.
8. Chen, W., and R. C. Lee. 1994. Altered ion channel conductance and ionic selectivity induced by large imposed membrane potential pulse. *Biophys. J.* 67:603–612.
9. Bier, M., S. M. Hammer, D. J. Canaday, and R. C. Lee. 1999. Kinetics of sealing for transient electropores in isolated mammalian skeletal muscle cells. *Bioelectromagnetics.* 20:194–201.
10. Gabriel, B., and J. Teissie. 1997. Direct observation in the millisecond time range of fluorescent molecule asymmetrical interaction with the electropermeabilized cell membrane. *Biophys. J.* 73:2630–2637.
11. Gabriel, B., and J. Teissie. 1998. Mammalian cell electropermeabilization as revealed by millisecond imaging of fluorescence changes of ethidium bromide in interaction with the membrane. *Bioelectrochem. Bioenerg.* 47:113–118.
12. Gowrishankar, T. R., W. Chen, and R. C. Lee. 1998. Non-linear microscale alterations in membrane transport by electropermeabilization. *Ann. N. Y. Acad. Sci.* 858:205–216.
13. Johnsson, M., M. Silvander, G. Karlsson, and K. Edwards. 1999. Effect of PEO-PPO-PEO triblock copolymers on structure and stability of phosphatidylcholine liposomes. *Langmuir.* 15:6314–6325.
14. Kostarelos, K., P. F. Luckham, and T. F. Tadros. 1995. Addition of block copolymers to liposomes prepared using soybean lecithin. Effects on formation, stability and the specific localization of the incorporated surfactants investigated. *J. Liposome Res.* 5:117–130.
15. Kostarelos, K., M. Kipps, T. F. Tadros, and P. F. Luckham. 1998. Molecular structure and conformation in phospholipid vesicles sterically stabilized by (tri)-block copolymers investigated by multinuclear magnetic resonance techniques. *Colloids Surf.* 136:1–9.
16. Kostarelos, K., P. F. Luckham, and T. F. Tadros. 1998. Steric stabilization of phospholipid vesicles by block copolymers. Vesicle flocculation and osmotic swelling caused by monovalent and divalent cations. *J. Chem. Soc. Faraday Trans.* 94:2159–2168.
17. Kostarelos, K., T. F. Tadros, and P. F. Luckham. 1999. Physical conjugation of (tri-)block copolymers to liposomes toward the construction of sterically stabilized vesicle systems. *Langmuir.* 15:369–376.
18. Woodle, M. C., M. S. Newman, and F. J. Martin. 1992. Liposome leakage and blood circulation: comparison of adsorbed block copolymers with covalent attachment of PEG. *Int. J. Pharm.* 88:327–334.
19. Padanilam, J. T., J. C. Bischof, R. C. Lee, E. G. Cravalho, R. G. Tompkins, M. L. Yarmush, and M. Toner. 1994. Effectiveness of poloxamer 188 in arresting calcein leakage from thermally damaged isolated skeletal muscle cells. *Ann. N. Y. Acad. Sci.* 720:111–123.
20. Hannig, J., D. Zhang, D. J. Canaday, M. A. Beckett, R. D. Astumian, R. Weichselbaum, and R. C. Lee. 2000. Surfactant sealing of membranes permeabilized by ionizing radiation. *Radiat. Res.* 154:171–177.
21. Orringer, E. P., J. F. Casella, K. I. Ataga, M. Koshy, P. Adams-Graves, L. Luchtman-Jones, T. Wun, M. Watanabe, F. Shafer, A. Kutlar, M. Abboud, M. Steinberg, B. Adler, P. Swerdlow, C. Terregino, S. Saccente, B. Files, S. Ballas, R. Brown, S. Wojtowicz-Praga, and J. M. Grindel. 2001. Purified poloxamer 188 for treatment of acute vaso-occlusive crisis of sickle cell disease: a randomized controlled trial. *JAMA.* 286:2099–2106.
22. Maskarinec, S. A., J. Hannig, R. C. Lee, and K. Y. C. Lee. 2002. Direct observation of poloxamer 188 insertion into lipid monolayers. *Biophys. J.* 82:1453–1459.
23. Maskarinec, S. A., and K. Y. C. Lee. 2003. Comparative study of poloxamer insertion into lipid monolayers. *Langmuir.* 19:1809–1815.
24. Shaikh, S. R., A. C. Dumaual, L. J. Jenski, and W. Stillwell. 2001. Lipid phase separation in phospholipid bilayers and monolayers modeling the plasma membrane. *Biochim. Biophys. Acta.* 1512:317–328.
25. Marsh, D. 1996. Lateral pressure in membranes. *Biochim. Biophys. Acta.* 1286:183–223.
26. Als-Nielsen, J., and K. Kjaer. 1989. X-ray reflectivity and diffraction studies of liquid surfaces and surfactant monolayers. *In* The Proceedings of the NATO Advanced Study Institute, Phase Transitions in Soft Condensed Matter, Geilo, Norway, April 4–14. Plenum Publishing, New York. 113–138.
27. Als-Nielsen, J., D. Jacquemain, K. Kjaer, F. Leveiller, M. Lahav, and L. Leiserowitz. 1994. Principles and applications of grazing incidence X-ray and neutron scattering from ordered molecular monolayers at the air-water interface. *Phys. Rep.* 246:251–313.
28. Kaganer, V. M., H. Möhwald, and P. Dutta. 1999. Structure and phase transitions in Langmuir monolayers. *Rev. Mod. Phys.* 71:779–819.
29. Jensen, T. R., and K. Kjaer. 2001. Structural properties and interactions of thin films at the air-liquid interface explored by synchrotron x-ray scattering. *In* Novel Methods to Study Interfacial Layers. R. Miller, editor. Elsevier, Amsterdam. 205–254.
30. Wu, G., J. Majewski, C. Ege, K. Kjaer, M. J. Weygand, and K. Y. C. Lee. 2004. Lipid corralling and poloxamer squeeze-out in membranes. *Phys. Rev. Lett.* 93:028101–028104.
31. Gopal, A., and K. Y. C. Lee. 2001. Morphology and collapse transitions in binary phospholipid monolayers. *J. Phys. Chem. B.* 105: 10348–10354.
32. Majewski, J., R. Popovitz-Biro, W. G. Bouwman, K. Kjaer, J. Als-Nielsen, M. Lahav, and L. Leiserowitz. 1995. The structural properties of uncompressed crystalline monolayers of alcohols $CH_{2n+1}OH$ (n = 13–31) on water and their role as ice nucleators. *Chem.* 1:304–312.
33. Weissbuch, I., R. Popovitz-Biro, M. Lahav, L. Leiserowitz, K. Kjaer, and J. Als-Nielsen. 1997. Molecular self-assembly into crystals at air-liquid interfaces. *Adv. Chem. Phys.* 102:39–102.

34. Lee, K. Y. C., J. Majewski, T. L. Kuhl, P. B. Howes, K. Kjaer, M. M. Lipp, A. J. Waring, J. A. Zasadzinski, and G. S. Smith. 2001. Synchrotron x-ray study of lung surfactant-specific protein SP-B in lipid monolayers. *Biophys. J.* 81:572–585.

35. Kjaer, K. 1994. Some simple ideas on x-ray reflection and grazing-incidence diffraction from thin surfactant films. *Physica B (Amsterdam).* 198:100–109.

36. Braslau, A., M. Deutsch, P. S. Pershan, A. H. Weiss, J. Als-Nielsen, and J. Bohr. 1985. Surface roughness of water measured by x-ray reflectivity. *Phys. Rev. Lett.* 54:114–117.

37. Pershan, P. S. 1990. Structure of surfaces and interfaces as studied using synchrotron radiation. *Faraday Discuss. Chem. Soc.* 89:231–245, 248–250,255.

38. Jensen, T. R., K. Balashev, T. Bjornholm, and K. Kjaer. 2001. Novel methods for studying lipids and lipases and their mutual interaction at interfaces. Part II. Surface sensitive synchrotron X-ray scattering. *Biochimie.* 83:399–408.

39. Guinier, A. 1963. X-ray Diffraction: Freeman, San Francisco.

40. Hahn, T., editor. 1987. International Tables for Crystallography. Reidel, Dordrecht, The Netherlands.

41. Brezesinski, G., A. Dietrich, B. Struth, C. Böhm, W. G. Bouwman, K. Kjaer, and H. Möhwald. 1995. Influence of ether linkages on the structure of double-chain phospholipid monolayers. *Chem. Phys. Lipids.* 76:145–157.

42. Lee, K. Y. C., A. Gopal, A. Von Nahmen, J. A. Zasadzinski, J. Majewski, G. S. Smith, P. B. Howes, and K. Kjaer. 2002. Influence of palmitic acid and hexadecanol on the phase transition temperature and molecular packing of dipalmitoylphosphatidylcholine monolayers at the air-water interface. *J. Chem. Phys.* 116: 774–783.

43. Schalke, M., P. Krüger, M. Weygand, and M. Lösche. 2000. Submolecular organization of DMPA in surface monolayers beyond the two-layer model. *Biochim. Biophys. Acta.* 1446:113–126.

44. Armen, R. S., O. D. Uitto, and S. E. Feller. 1998. Phospholipid component volumes: determination and application to bilayer structure calculations. *Biophys. J.* 75:734–744.

45. Nagle, J. F., and M. C. Wiener. 1988. Structure of fully hydrated bilayer dispersions. *Biochim. Biophys. Acta.* 942:1–10.

46. Schalke, M. 2000. Konformation und Hydratation von Phospholipiden in Oberflächenmonoschichten: Röntgenreflexion und IR-Spektroskopie Ph.D. thesis. Universität Leipzig, Leipzig, Germany.

47. Vaknin, D., P. Krüger, and M. Lösche. 2003. Anomalous X-ray reflectivity characterization of ion distribution at biomimetic membranes. *Phys. Rev. Lett.* 90:178102.

48. Brun, A., G. Brezesinski, H. Mohwald, M. Blanzat, E. Perez, and I. Rico-Lattes. 2003. Interaction between phospholipids and new Gemini catanionic surfactants having anti-HIV activity. *Colloids Surf. A.* 228: 3–16.

49. Castile, J. D., K. M. G. Taylor, and G. Buckton. 2001. The influence of incubation temperature and surfactant concentration on the interaction between dimyristoylphosphatidylcholine liposomes and poloxamer surfactants. *Int. J. Pharm.* 221:197–209.

50. Lee, R. C., A. Myerov, and C. P. Maloney. 1994. Promising therapy for cell membrane damage. *Ann. N. Y. Acad. Sci.* 720:239–245.

51. Jamshaid, M., S. J. Farr, P. Kearney, and I. W. Kellaway. 1988. Poloxamer sorption on liposomes: comparison with polystyrene latex and influence on solute efflux. *Int. J. Pharm.* 48:125–131.

52. Moghimi, S. M., C. J. H. Porter, L. Illum, and S. S. Davis. 1991. The effect of poloxamer-407 on liposome stability and targeting to bone marrow: comparison with polystyrene microspheres. *Int. J. Pharm.* 68: 121–126.

53. Silvestro, L., and P. H. Axelsen. 1998. Infrared spectroscopy of supported lipid monolayer, bilayer and multibilayer membranes. *Chem. Phys. Lipids.* 96:69–80.

54. Vineyard, G. H. 1982. Grazing-incidence diffraction and the distorted-wave approximation for the study of surfaces. *Phys. Rev. B.* 26:4146–4159.